Assimilation of production and EM data

Data assimilation for geothermal doublets using production data and electromagnetic observations

by

C. Oudshoorn

to obtain the degree of Master of Science
at the Delft University of Technology,
to be defended publicly on Friday August 18, 2023 at 14:00 AM.

Student number:	4925742	
Project duration:	March 1, 2023 – August 18, 2023	
Thesis committee:	Dr. D. Voskov,	TU Delft, supervisor
	Prof. dr. E. C. Slob,	TU Delft, supervisor
	Dr. C. Schmelzbach,	ETH Zurich

This thesis is confidential and cannot be made public until February 11, 2024.

Data assimilation for geothermal doublets using production data and electromagnetic observations

Christiaan Oudshoorn*, Dieter Werthmüller, Evert Slob, Denis Voskov

ABSTRACT

The data assimilation process for geothermal reservoirs often relies on well data which primarily offers insights into the immediate vicinity of the borehole. However, integrating geophysical methods can provide valuable information beyond well proximity, possibly enhancing reservoir predictions. Electromagnetic methods can be sensitive to the decreasing conductivity from heat extraction in geothermal reservoirs. A scheme to incorporate electromagnetic data into a data assimilation process for geothermal reservoirs is presented and implemented in this study. First, an ensemble of prior models representing the reservoir uncertainty is used to determine the moments of the resulting temperature field using a forward geothermal simulation. Source and receiver locations are determined by maximizing the distance of the path through the expected temperature changes while ensuring that the source and receiver are not excessively distant. Subsequently, a conductivity model is implemented using an empirical relationship. The expected electric field response can then be simulated using an electromagnetic forward model. To assimilate the data, the Ensemble Smoother with the Multiple Data Assimilation (ES-MDA) method is employed. The findings demonstrate that the incorporation of electromagnetic data provides more information regarding the temperature field, which when combined with the localized data from the production well improves the temperature forecast accuracy of both the production well and the entire reservoir model.

INTRODUCTION

Geothermal energy holds immense potential as a clean, renewable, and sustainable energy source (Hackstein and Madlener, 2021). Realizing the full benefits of this resource requires a profound comprehension of the subsurface reservoirs containing geothermal energy, and numerical simulation stands as a powerful approach to achieve this understanding (Tian et al., 2023).

The calibration of physical reservoir models to match actual field measurements is fundamental to this endeavor. This process, commonly referred to as “history matching” or “data assimilation”, aims to adjust the reservoir model to replicate the observed field measurements (Huseby et al., 2013; Wu et al., 2021). However, assimilation schemes relying solely on well data, such as temperature and borehole pressure, suffer from limited information content, offering insights predominantly within the immediate vicinity of the boreholes (Zhang et al., 2020).

Geophysical measurements can address this limitation by providing valuable supplementary information concerning dynamic changes in the reservoir beyond the direct well proximity (Zhang and Hoteit, 2021; Djuraev et al., 2017; Sambo et al., 2020; Bretaudeau et al., 2021). Of particular interest, EM methods exhibit sensitivity to conductivity changes associated with fluid temperature fluctuations (Ucok et al., 1980; Sen and Goode, 1992).

This paper delves into the integration of EM data within a data assimilation framework, alongside well data, to enhance the reservoir characterization. First, the method for creating a model ensemble is described, which is the collection of models which together describe the reservoir uncertainty. Thereafter, descriptions of the reservoir, rock physics, and EM forward models are given. After this, the method for the data assimilation and method for determining EM source and receiver locations are described. Lastly, a numerical example is presented where EM data is incorporated into a data assimilation scheme to predict reservoir performance and the results are evaluated.

---

*Delft University of Technology, 2628 CN Delft, The Netherlands
E-mail addresses:
ChrisXPS@protonmail.com, D.Werthmuller@tudelft.nl, E.C.Slob@tudelft.nl, D.V.Voskov@tudelft.nl

THEORY

Ensemble Generation

The initial phase of the workflow involves the generation of an ensemble to capture the uncertainty associated with reservoir parameters. In this paper, the focus is on the Delft sandstone member, which has a considerable geothermal energy potential (Donselaar et al., 2015).

The ensemble is designed to reflect the characteristics of the Delft reservoir, which has a normally distributed porosity with a mean of 0.2192 and a standard deviation of 0.0891. Each member of the ensemble comprises a grid of 140 by 140 blocks, where each grid block measures 20 by 20 m with a 100 m thickness. To create the ensemble members, sequential Gaussian simulation is employed. A total of 25 random grid blocks are assigned a random value from the aforementioned probability distribution for each realization. Values between these blocks are then estimated sequentially in a random order using a correlation defined by a spherical variogram,

$$c \cdot \mathrm{Sph}\left(\frac{h_d}{a_r}\right) = \begin{cases} c \cdot \left[1.5\frac{h_d}{a_r} - 0.5\left(\frac{h_d}{a_r}\right)^3\right], & \text{if } h \leq a \\ c, & \text{if } h \geq a \end{cases}, \tag{1}$$

where h_d is the distance in m from the nearest value, a_r is the range in m beyond which there is no correlation, and c is the sill (Deutsch and Journel, 1992). The sill represents the global maximum semivariance. In this paper, a range of 1000 m and a sill of 1 is used. The geostatistical package *GeoStatPy* for Python is employed to facilitate this process (Pyrcz et al., 2021).

An empirical relationship is used to calculate the corresponding permeability, specifically $\mu_h = 196449\phi^{4.3762}$, where μ_h is the hydraulic permeability in mD and ϕ is the porosity. Lastly, the porosity was limited to be within 0.05 and 0.40. The injection well grid block, located on index $i_x = 40$ and $i_y = 70$, and the production well grid block, located on $i_x = 100$ and $i_y = 70$, are limited to having a permeability between 800 and 1000 mD.

Reservoir Simulation

This paper employs the reservoir simulation approach based on the work by Khait and Voskov (2018); Wang et al. (2020) and utilizes the Delft Advanced Research Terra Simulator (DARTS). This approach focuses on two-phase thermal simulation with water, considering its governing equations and nonlinear formulations. However, this paper considers a low enthalpy system, and for this reason, the governing equations are adapted to account for a single phase.

The mass equation of this system is described by

$$\frac{\partial}{\partial t}(\phi\rho) - \nabla\cdot(\rho u) + \rho\tilde{q} = 0, \tag{2}$$

and the energy conservation equation of this system by

$$\begin{aligned} &\frac{\partial}{\partial t}(\phi\rho U) + \frac{\partial}{\partial t}((1-\phi)U_r) \\ &- \nabla\cdot(h\rho u) + \nabla\cdot(\kappa\nabla T) + h\rho\tilde{q} = 0. \end{aligned} \tag{3}$$

In the above equations, t represents time in seconds, ρ signifies fluid density in kmol/m^3, $\tilde{q}$ represents the fluid source rate per unit volume in m^3/s, U indicates specific fluid internal energy in kJ/kmol, U_r indicates the rock internal energy in kJ/m^3, h denotes fluid enthalpy in kJ/kmol, κ represents thermal conduction in W/m/K, and T signifies temperature in K.

Furthermore, the fluid Darcy velocity u_d in m/s, considering gravity effects can be defined as

$$u_d = \mathbf{K}\frac{1}{\mu}\left(\nabla P - \gamma\nabla D\right). \tag{4}$$

Here, $\mathbf{K}$ represents the permeability tensor of the media in mD, μ represents the fluid viscosity in Pa·s, P denotes the pressure in bars, γ represents the specific weight in N/m^3, and D signifies the depth in m. The rock compressibility can be incorporated into the porosity using $\phi = \phi_0\left(1 + c_r\left(P - P_{ref}\right)\right)$, where ϕ_0 represents the initial porosity, c_r represents the compressibility of the porous media in 1/bars, and P_{ref} is the reference pressure in bars.

In a geothermal system where the only component is water, pressure and enthalpy are considered primary variables in DARTS. To linearize the nonlinear system of equations, the Newton-Raphson method is adopted. The resulting system is expressed as:

$$\mathbf{J}\left(\omega^k\right)\left(\omega^{k+1} - \omega^k\right) + r\left(\omega^k\right) = 0, \tag{5}$$

where $\mathbf{J}\left(\omega^k\right)$ is the Jacobian matrix and $r\left(\omega^k\right)$ is the residual, with k defining the iteration. The state variables of enthalpy and pressure are encapsulated and represented by ω. An initial time step of 10^{-3} days is used, with a maximum time step of 365 days with the time step increasing by 8 times as long as the solution is converging, for the duration of the reservoir simulation.

To improve the computational process and flexibility of nonlinear formulation, the operator-based linearization (OBL) technique is employed, as proposed by Khait and Voskov (2017). In this approach, the discretized mass and energy conservation equations are transformed into an operator form, separating the space- and state-dependent properties. The state-dependent operators are then parameterized in the space of nonlinear variables adaptively using a limited number of supporting points. This improves the speed and robustness of highly nonlinear reservoir simulation.

Rock-Physics Model

To model the EM response from the rock properties and dynamic changes, a rock physics relationship is required linking the reservoir parameters to conductivity. As hot water is extracted from the geothermal reservoir and cold water is injected, the temperature within the reservoir decreases. Over time, this forms a cold plume which progresses from the injection well to the production well.

Multiple studies have been conducted on measuring the change in conductivity as the temperature of a brine-saturated rock sample changes with varying degrees of complexity. Ucok et al. (1980) described an empirical relationship linking temperature and ions within the brine with conductivity, and Sen and Goode (1992) derived an empirical relationship that incorporates the inclusion of clay minerals.

For simplicity, however, the approach by Dresser Industries (1982) is used, which simply links salt concentration and temperature to electrical conductivity. Differences in estimated conductivities among the above-mentioned methods are generally small, with the exception that the inclusion of clay minerals leads to a reduction in the change in conductivity with varying temperatures.

Assuming that the main electrical conductive feature in the reservoir rock is the pore fluid, Archie's law is used to determine the conductivity of the rock

$$\sigma = a^{-1}\sigma_w \phi^m s_w^n, \tag{6}$$

where σ is the formation conductivity in S, and σ_w is the brine conductivity in S. The saturation s_w is set to 1 as only one fluid is considered. Moreover, a, m, and n are Archie's parameters which depend on the rock's cementation, wettability, compaction, and pore structure.

The brine conductivity σ_w can be determined by the empirical relationship:

$$\sigma_w = \left[\left(0.0123 + \frac{3647.5}{C_w^{0.955}}\right)\frac{82}{1.8T+39}\right]^{-1}, \tag{7}$$

where C_w is the salt concentration in ppm. The salt concentration is assumed to remain constant at 100,000 ppm and the temperature is retrieved from the reservoir simulation to determine the conductivity at each grid cell. It should be noted that Archie's law is an empirical law for clean sandstones (Archie, 1942). For reservoir models which include other facies, an additional method has to be used.

Electromagnetic Modeling

This paper employs the *emg3d* three-dimensional electromagnetic (EM) modeller, which is a Python package specifically suited for diffusion EM modeling (Werthmüller et al., 2019). The response from the EM method is governed by Maxwell's equations (Zhang et al., 2020). In the presence of a current source $\mathbf{J}_s$ and under the diffusive field approximation, Maxwell's equations can be given as

$$\begin{aligned} \partial_t \mathbf{B}(\mathbf{x},t) + \nabla \times \mathbf{E}(\mathbf{x},t) &= 0 \\ \nabla \times \mathbf{H}(\mathbf{x},t) - \mathbf{J_c}(\mathbf{x},t) &= \mathbf{J_s}(\mathbf{x},t), \end{aligned} \tag{8}$$

where $\mathbf{J}_s$ is in A, $\mathbf{E}(\mathbf{x},t)$ is the electrical field in V/m, and $\mathbf{H}(\mathbf{x},t)$ is the magnetic field in A/m (Werthmüller et al., 2019).

The conduction current is defined such that is obeys Ohm's law as

$$\mathbf{J}_c = \sigma(\mathbf{x})\mathbf{E}(\mathbf{x},t), \tag{9}$$

and the magnetic induction is defined as

$$\mathbf{B}(\mathbf{x},t) = \mu_m \mathbf{H}(\mathbf{x},t). \tag{10}$$

Here the magnetic permeability μ_m in H/m is expressed as $\mu_m = \mu_r\mu_0$, where μ_r and μ_0 are the relative and vacuum magnetic permeability respectively.

In this paper, the relative permeability μ_r is set to 1. Eliminating the magnetic field from Equation 8 yields the second-order parabolic system of equations given as

$$\sigma\partial_t \mathbf{E} + \nabla \times \mu_0^{-1} \nabla \times \mathbf{E} = -\partial_t \mathbf{J}_\mathrm{s}. \tag{11}$$

Using the Fourier transform both the electrical $\mathbf{E}(\mathbf{x},t)$ and magnetic field $\mathbf{H}(\mathbf{x},t)$ can be brought into the frequency domain, yielding

$$\mathrm{i}\omega\mu_0\sigma\hat{\mathbf{E}} = -\mathrm{i}\omega\mu_0\hat{\mathbf{J}}_s. \tag{12}$$

Lastly, a perfectly electrically conducting boundary can be used such that $\mathbf{n}\times\mathbf{E} = 0 \quad$ and $\quad \mathbf{n}\cdot\mathbf{H} = 0$ where $\mathbf{n}$ is the outward normal vector on the boundary of the computational domain.

Since the current source $\mathbf{J}_s$ used is a 1 m long 1 A electric dipole and the conductivity model $\sigma(\mathbf{x})$ is retrieved from the reservoir model, only the electric field $\mathbf{E}$ has to be solved for (Zhang et al., 2020). Lastly, a sampling operator $\mathbf{S}(\cdot)$ that samples the electric field $\mathbf{E}$ at receiver locations to get the observed data $\mathbf{d}_{obs}$ is given by:

$$\boldsymbol{d}_\mathrm{obs} = \left|\mathbf{S}\left(\boldsymbol{x}_s, \boldsymbol{x}_r\right)\right|, \tag{13}$$

where $\boldsymbol{x}_s$ represents the source locations, and $\boldsymbol{x}_r$ the receiver locations. The modulus is taken to take the amplitude of the electric field $\mathbf{E}$, and to avoid complex numbers in the measured data.

The EM forward model requires a three-dimensional grid, while the conductivity model is two-dimensional. For compatibility, the conductivity model is extrapolated in the z-axis, while the x- and y-axis are given buffer cells of 1 S around the model. The amount of buffer cells in each direction is calculated based on the frequency and aforementioned buffer conductivity, to avoid boundary effects.

Data Assimilation Scheme

The Ensemble Smoother for Multiple Data Assimilation (ES-MDA) method (Emerick and Reynolds, 2013) is used in this paper to improve model predictions by incorporating observation data. ES-MDA employs an ensemble of models to capture inherent uncertainty, advancing them in time using model equations, reflecting the range of potential outcomes due to uncertainty in initial conditions and model parameters. This approach focuses on parameter estimation leveraging the stability of reservoir simulation models in relation to the rock reservoir fields.

To update the model, the ES-MDA method considers several factors. These include the discrepancy between the predicted and measured data, the cross-covariance between the model parameters and predicted data, the auto-covariance of the predicted data, and the covariance matrix of observed measurement orders.

This process constitutes the ensemble smoother component of ES-MDA. However, this approach can be seen as equivalent to a single Gauss-Newton iteration. To potentially achieve better convergence, ES-MDA incorporates multiple data assimilation by inflating the covariance matrix associated with measurement errors. By performing several smaller iterations instead of one large correction, the method aims to refine the parameter estimation further, ultimately improving the convergence of the assimilation process.

The ES-MDA analysis equation is given by:

$$\mathbf{m}_j^a = \mathbf{m}_j^f + \mathbf{C}_{\mathrm{MD}}^f \left(\mathbf{C}_{\mathrm{DD}}^f + \alpha_i \mathbf{C}_{\mathrm{D}}\right)^{-1} \left(\mathbf{d}_{\mathrm{uc},j} - \mathbf{d}_j^f\right), \quad (14)$$

for $j = 1, 2, \ldots N_e$, where N_e is the number of ensemble realizations. Moreover, $\mathbf{C}_{\mathrm{MD}}$ represents the cross-covariance matrix of the model parameters $\mathbf{m}$ and the predicted data $\mathbf{d}$, $\mathbf{C}_{\mathrm{DD}}$ is the $N_d \times N_d$ auto-covariance matrix of the predicted data with N_d representing the number of observed data, and $\mathbf{C}_{\mathrm{D}}$ is the $N_d \times N_d$ covariance matrix of measurement errors. The superscript a and f are the analysis and forecast respectively. In this paper, porosity is taken as the model parameter and temperature and pressure at the production well, and electric field amplitude at the receiver, are taken as observation data. The electric field amplitude measurements in particular are also scaled by a constant, to bring them closer to the magnitude of the other production well measurements.

Lastly, $\mathbf{d}_{\mathrm{uc}}$ is defined as:

$$\mathbf{d}_{\mathrm{uc}} = \mathbf{d}_{\mathrm{obs}} + \sqrt{\alpha_i} \mathbf{C}_{\mathrm{D}}^{1/2} \mathbf{Z}_d, \quad (15)$$

where $\mathbf{d}_{\mathrm{obs}}$ is the observed data, $\mathbf{Z}_d$ is a $N_d \times N_e$ matrix composed of random samples drawn from a normal Gaussian distribution, and α_i is the magnitude of perturbation applied to the observations. It has to satisfy the condition that $\sum_{i=1}^{N_a} \frac{1}{\alpha_i} = 1$, but is otherwise a user set parameter.

The ES-MDA algorithm can be summarized as follows:

1. Determine the number of data assimilations N_a and the coefficients α_i for $i = 1, \ldots, N_a$.
2. For each data assimilation iteration $i = 1$ to N_a:
    - Run the entire ensemble from time 0
    - Perturb the observations with Equation 15
    - Update the ensemble using Equation 14

RESULTS

EM Observation Well Placement

The change in reservoir conductivity resulting from geothermal energy extraction is expected to only be a few S at most, making it challenging for surface-based EM receivers to detect this change. For example, the Delft reservoir considered in this paper has an overburden depth of 2000 m (Vardon et al., 2020).

Placing receivers in boreholes at the desired depth is a costly solution. Therefore, careful consideration must be given to receiver placement to maximize the benefits from each observation well. Since transmitting current to reservoir depth is difficult, the sources are positioned on the surface.

To simulate the conductivity field before and after injection, each ensemble member was simulated for 25 years using the reservoir forward model with an initial temperature of 348.15 K and an injection temperature of 308.15 K, thermal conductivity of 2.1 W/m/K, and injection rate of 0.0579 m^3/s. The injection well pressure is set to 300 bars, production well pressure to 50 bars, and the initial pressure of the reservoir is at 200 bars. The injection well is placed at $x = 800$ and $y = 1400$ m, and the production well is positioned at $x = 2000$ and $y = 1400$ m.

Figures 1a and 1b illustrate an example of the resulting conductivity field for a single ensemble member before and after the simulation. Figures 1c and 1d illustrate the conductivity and temperature difference. Here it is seen that as the cold front infiltrates the reservoir, it leaves an imprint in the conductivity field of around 0 to 1 S. Since the pore fluid is the primary conductor, the decrease in conductivity also reflects the porosity.

The corresponding electric field amplitudes are shown in Figures 2a and 2b, respectively. The ratio of the two electrical fields is presented in Figure 2c to better highlight the impact of conductivity changes on the electric field amplitude. The decreased conductivity leads to a modified electric field amplitude since the electric field $\mathbf{E}$ is allowed to penetrate deeper into the reservoir due to reduced current loss in highly conductive zones.

Optimizing the mean and standard deviation of the electrical field amplitude at a receiver to their highest values is crucial for ensuring that the data assimilation attains the most accurate solution. To determine the best source location, the mean and standard deviation of the electric field amplitude for three different sources were simulated: within, on the boundary, and far outside the cold plume.

Figures 3a, 3b, 3c, and 3d present the mean temperature field of the ensemble along with the mean electrical field amplitude ratio for these locations. It is observed that increasing the distance that the electrical field $\mathbf{E}$ has to travel through the temperature plume, increases the mean maximum change in the electrical field amplitude. Reducing the distance between the source and the expected boundary of the temperature plume results in a more significant decrease in the electrical field amplitude change. This indicates that the source should be along the expected temperature plume.

Additionally, Figures 4a, 4b, 4c, and 4d demonstrate the standard deviation of both the temperature field and electrical field amplitude ratio for three different source locations. The highest change in the standard deviation of the electrical field amplitude is seen when the source is placed close to the expected temperature plume, either inside it or right outside the boundary. Placing the source far from the temperature change limits both the intensity and range of the deviations amongst ensemble members.

From this, it is deduced that the optimal source and receiver placement are achieved by placing them on the two opposite sides of the expected temperature plume. Since the receiver is in a fixed location it is ideally placed in a location which always borders the expected cold plume.

These findings also underscore the importance of accurately capturing uncertainty in the prior ensemble models, as the optimal source and receiver setup relies on the expected moments of the temperature plume uncertainty.

Data Assimilation of EM Data

The data assimilation training spanned 25 years with a five-year measurement interval, which was chosen due to the high computational cost of the EM forward model and measurement consistency. Temperature and pressure measurements were sampled at the production well. An additional EM receiver well was placed at (x = 1400, y = 1400 m, z = -2050 m), and the vertical electrical field amplitude at the receiver was sampled at the same five-year intervals, scaled by multiplying it by 10^{14} to increase the impact of EM observations. Five source locations were used: (400, 1000), (400, 1400), (400, 1800), (1000, 1000), and (1000, 1800). The change over time of all observations is also utilized, calculated by taking the change in observations divided by the change in time between consecutive sampling times.

The data assimilation process comprised six steps, with the α_i values being 1/0.02, 1/0.05, 1/0.08, 1/0.2, 1/0.3, and 1/0.4. This causes each subsequent data assimilation iteration to have a smaller covariance matrix, allowing for increasingly larger corrections. The prior ensemble consisted of the first 100 realizations, while the 101st is used as the reference model.

Three different scenarios were tested: one where only production well observations were used, one where both production well and EM observations were used, and one where only EM observations were used. The respective temperature results at the production well are given in Figures 5a, 5c, and 5e. Moreover, the difference between the final mean ensemble temperature field and reference final temperature field is shown in Figures 5b, 5d, and 5f. Reference production well observations were given a noise of 0.1%, and EM receiver measurements were given a noise of 1%.

The integration of both production well and EM observations has demonstrated substantial improvements in predicting the production well temperature and final temperature field. Solely relying on the point observations improves the prediction only at this specific point (e.g., at the production well). However, this approach performs poorly in predicting the spatial temperature distribution. Conversely, using only EM observations yields more precise predictions for the temperature field but performs poorly in predicting the temperature at the production well. By combining production well and EM observations we impose better constraints on the assimilated data which is indicated by the better data assimilation results.

The shape of the mismatch in Figures 5b, 5d, and 5f clearly indicates that the temperature variability is limited to a narrow "halo" around the temperature plume. This happens due to the Gaussian assumptions on the ensemble statistics and fixed injection rate control between different realizations. In more complex reservoir models, like fluvial systems, the cold plume between both wells can exhibit greater variability. EM observations could be especially useful in such systems due to their strength in constraining the expected temperature field.

CONCLUSION

We have demonstrated the effect of integrating electromagnetic observation data into a data assimilation scheme for geothermal reservoir forecasting of a temperature distribution. Additionally, we have established guidelines for determining the optimal source and receiver locations for electromagnetic measurements. Numerical experiment results have demonstrated that the change in conductivity caused by the cold water plume is substantial enough to be effectively quantified using EM measurements in a borehole with several electric current source locations on the ground surface. Moreover, by incorporating the temporal evolution of electric field amplitude into the data assimilation scheme, we have observed improvements in the accuracy of temperature forecasts. Specifically, the incorporation of electromagnetic data gives more information about the temperature field, which when combined with the more localized information from production well observations improves both the temperature forecast at the production well and final temperature field. Consequently, this method holds the potential to provide more precise constraints on the lifetime predictions of geothermal doublets and geothermal decision planning.

ACKNOWLEDGMENTS

The authors would like to thank Mahmoud Eltayieb, Gabriel Serrao Seabra, Alexandros Daniildis, and Aleks Novikov for fruitful discussions and support regarding various aspects of the forward models and assimilation scheme.

DATA AND MATERIALS AVAILABILITY

A copy of the scripts and model files utilized to create the results of this paper are given on the following repository:
github.com/Cioxss/EM_Assimilation

Figures

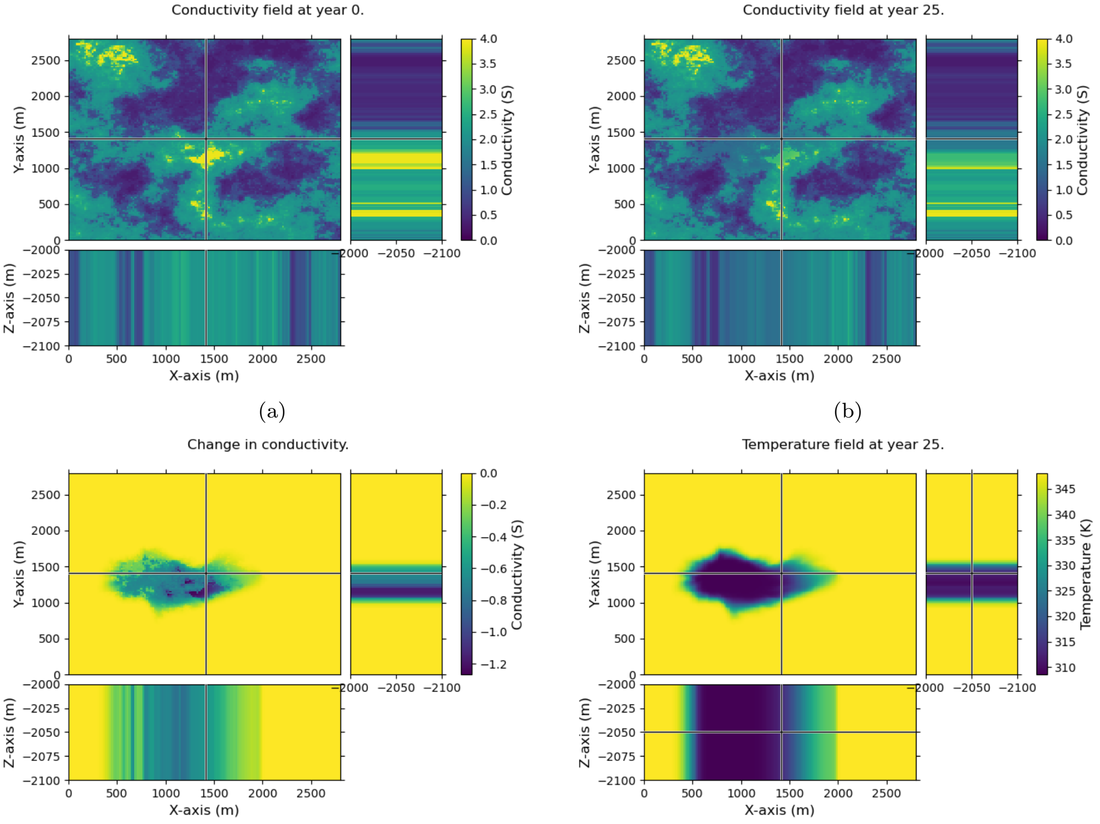

Conductivity field at year 0.

Conductivity field at year 25.

Change in conductivity.

Temperature field at year 25.

(a)

(b)

(c)

(d)

Figure 1: Changes of the conductivity field and temperature field over time. The conductivity field at year 0 in S (a), the conductivity field at year 25 in S (b), the difference between both conductivity fields in S (c), and the temperature field at year 25 in K (d).

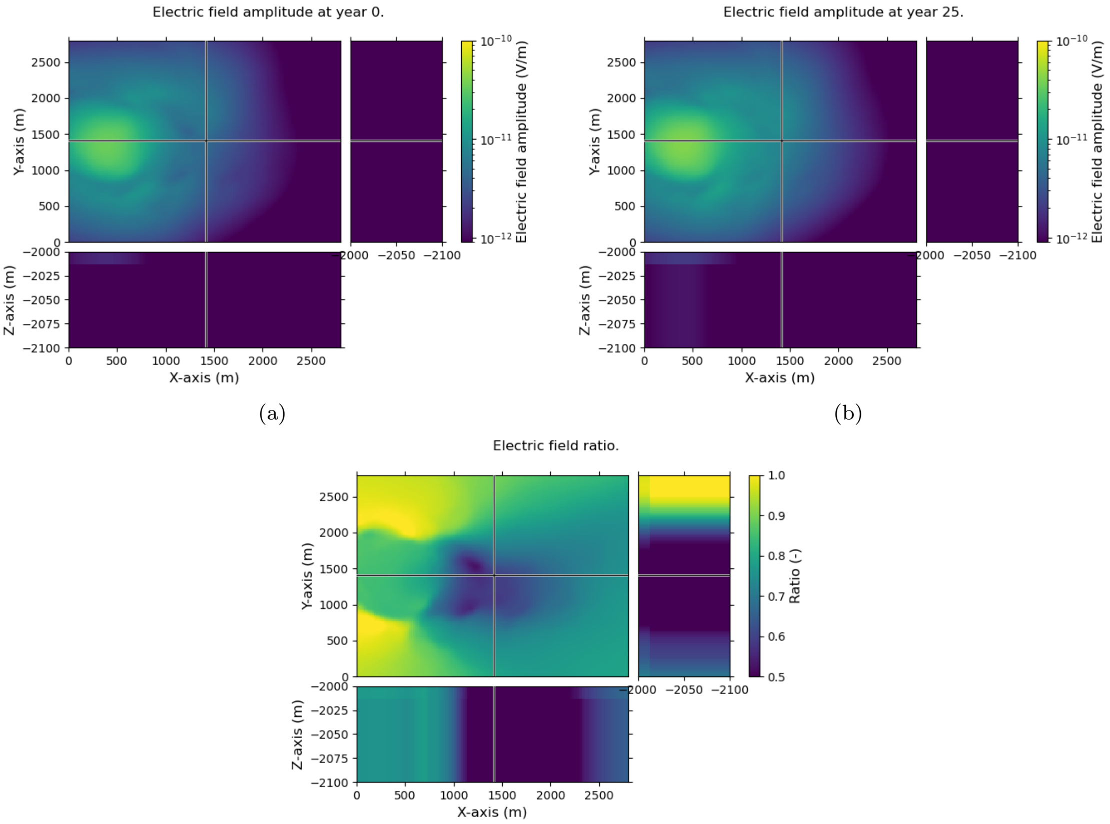

(a) (b)

(c)

Figure 2: Electric field amplitude of both conductivity fields of Figure 1, with the source placed at $x = 400$ and $y = 1400$. The electric field amplitude in V/m at year 0 (a), the electric field amplitude in V/m at year 25 (b), and the ratio between the electric field amplitude before and after 25 years (c).

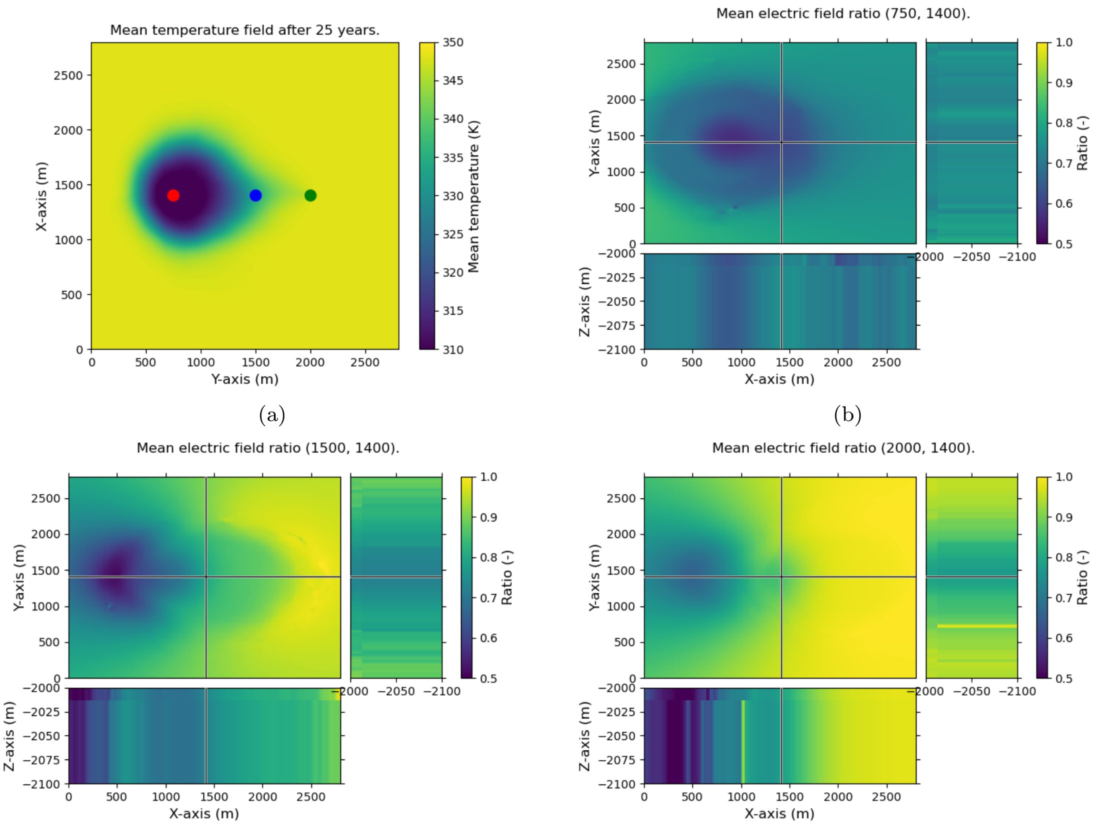

(a) (b)

(c) (d)

Figure 3: Mean temperature and electric field amplitude for the entire ensemble for three different source locations. The mean temperature in K of the entire ensemble in (a), the mean ratio of electrical field amplitudes in with the source placed at the red circle (b), the mean ratio of the electrical field amplitudes with the source placed at the blue circle (c), and the mean ratio of the electrical field amplitudes with the source placed at the green circle (d).

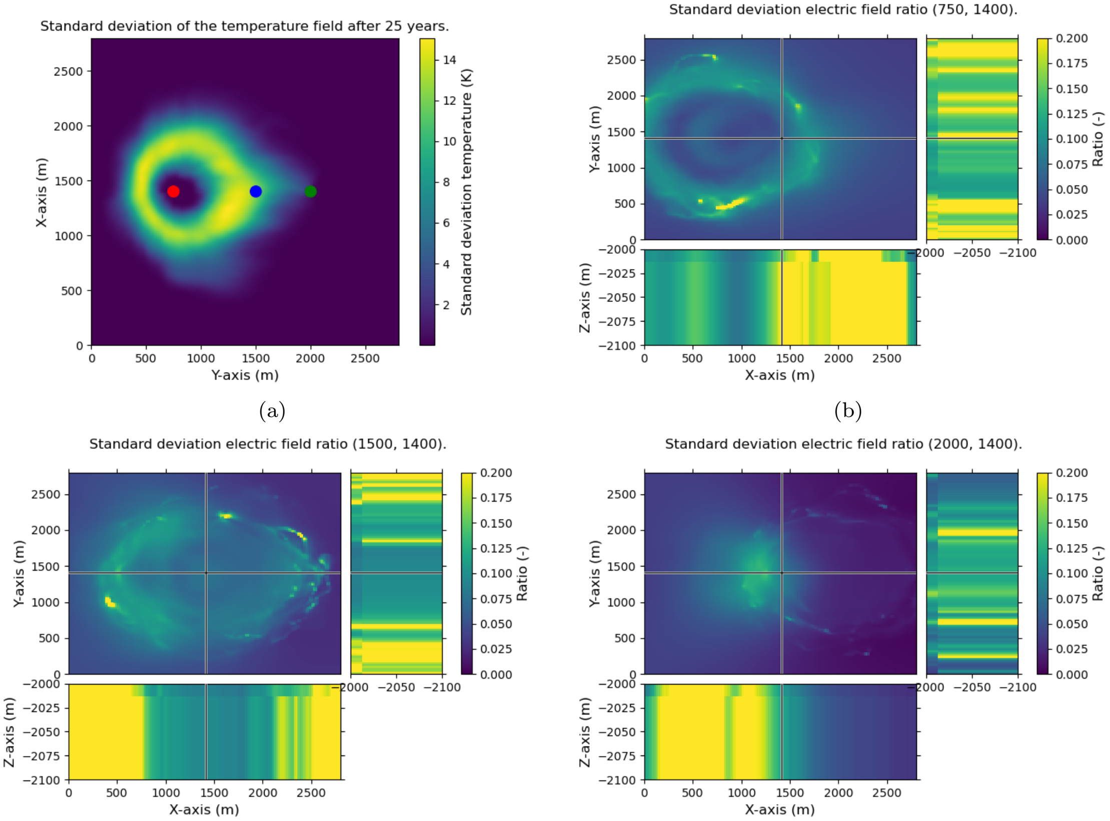

(a) (b)

(c) (d)

Figure 4: Standard deviation of the temperature and electric field amplitude for the entire ensemble and three different source locations. The standard deviation of the temperature in K of the entire ensemble (a), the standard deviation of the ratio of electrical field amplitudes with the source placed at the red circle (b), the standard deviation of the ratio of the electrical field amplitudes in with the source placed at the blue circle (c), and the standard deviation of the ratio of the electrical field amplitude with the source placed at the green circle (d).

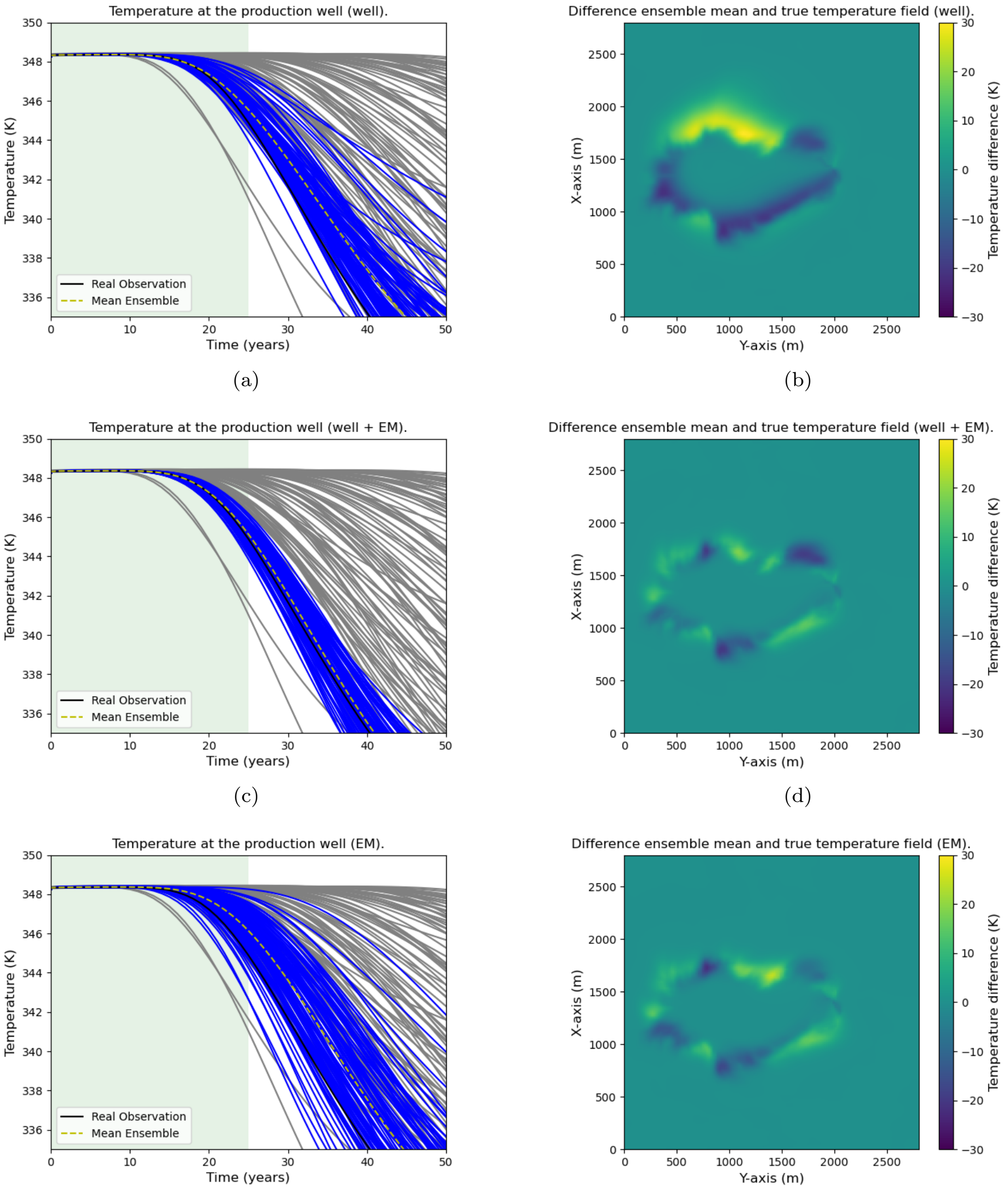

(a) (b) (c) (d) (e) (f)

Figure 5: Data assimilation results using either the production well observations, the EM observations, or both. The temperature at the product well, using only production well observations (a), and the difference between the true and ensemble mean final temperature field using only production well data (b). The temperature at the product well, using production well and EM observations (c), and the difference between the true and ensemble mean final temperature field using both (d). The temperature at the product well, using only EM observations (e), and the difference between the true and ensemble mean final temperature field using only EM observations (f). The green segment of the production well temperature plot represents the data assimilation training time, and the white area the prediction time. The grey lines represent the prior ensemble, with the blue lines the ensemble after data assimilation. The black line is the reference model observation and the dotted yellow line the ensemble mean.

REFERENCES

Archie, G. E., 1942, The electrical resistivity log as an aid in determining some reservoir characteristics: Transactions of the AIME, **146**, 54–62. (https://doi.org/10.2118/942054-G).

Bretaudeau, F., F. Dubois, S.-G. Bissavetsy Kassa, N. Coppo, P. Wawrzyniak, and M. Darnet, 2021, Time-lapse resistivity imaging: CSEM-data 3-D double-difference inversion and application to the Reykjanes geothermal field: Geophysical Journal International, **226**, 1764–1782. (https://doi.org/10.1093/gji/ggab172).

Deutsch, C., and A. Journel, 1992, GSLIB: Geostatistical Software Library and User's Guide: Oxford University Press. GSLIB: Geostatistical Software Library and User's Guide. (ISBN 9780195073928).

Djuraev, U., S. R. Jufar, and P. Vasant, 2017, A review on conceptual and practical oil and gas reservoir monitoring methods: Journal of Petroleum Science and Engineering, **152**, 586–601. (https://doi.org/10.1016/j.petrol.2017.01.038).

Donselaar, M., R. Groenenberg, and D. Gilding, 2015, Reservoir Geology and Geothermal Potential of the Delft Sandstone Member in the West Netherlands Basin: Presented at the Proceedings World Geothermal Congress 2015. (ISBN 978-1-877040-02-3).

Dresser Industries, 1982, Well logging and interpretation techniques: The course for home study: Dresser Atlas.

Emerick, A. A., and A. C. Reynolds, 2013, Ensemble smoother with multiple data assimilation: Computers & Geosciences, **55**, 3–15. (https://doi.org/10.1016/j.cageo.2012.03.011).

Hackstein, F. V., and R. Madlener, 2021, Sustainable operation of geothermal power plants: why economics matters: Geothermal Energy, **9**. (https://doi.org/10.1186/s40517-021-00183-2).

Huseby, O., R. Valestrand, G. Nævdal, and J. Sagen, 2013, Natural and Conventional Tracers for Improving Reservoir Models Using the EnKF Approach: SPE Journal, **15**. (https://doi.org/10.2118/121190-MS).

Khait, M., and D. Voskov, 2017, Operator-based linearization for general purpose reservoir simulation: Journal of Petroleum Science and Engineering, **157**. (https://doi.org/10.1016/j.petrol.2017.08.009).

———, 2018, Operator-based linearization for efficient modeling of geothermal processes: Geothermics, **74**, 7–18. (https://doi.org/10.1016/j.geothermics.2018.01.012).

Pyrcz, M., H. Jo, A. Kupenko, W. Liu, A. Gigliotti, T. Salomaki, and J. Santos, 2021, GeostatsPy python package: PyPI, Python Package Index. (https://pypi.org/project/geostatspy/).

Sambo, C., C. C. Iferobia, A. A. Babasafari, S. Rezaei, and O. A. Akanni, 2020, The Role of Time Lapse(4D) Seismic Technology as Reservoir Monitoring and Surveillance Tool: A Comprehensive Review: Journal of Natural Gas Science and Engineering, **80**, 103312. (https://doi.org/10.1016/j.jngse.2020.103312).

Sen, P. N., and P. A. Goode, 1992, Influence of temperature on electrical conductivity on shaly sands: Geophysics, **57**, 89–96. (https://doi.org/10.1190/1.1443191).

Tian, X., O. Volkov, and D. Voskov, 2023, An Advanced Inverse Modeling Framework for Efficient, Flexible, and Adjoint-Based History Matching of Geothermal Energy: SSRN Electronic Journal. (https://doi.org/10.2139/ssrn.4394926).

Ucok, H., I. Ershaghi, and G. R. Olhoeft, 1980, Electrical Resistivity of Geothermal Brines: Journal of Petroleum Technology, **32**, 717–727. (https://doi.org/10.2118/7878-PA).

Vardon, P., D. Bruhn, A. Steiginga, B. Cox, H. Abels, A. Barnhoorn, G. Drijkoningen, E. Slob, and K. Wapenaar, 2020, A Geothermal Well Doublet for Research and Heat Supply of the TU Delft Campus. (https://doi.org/10.48550/arXiv.2003.11826).

Wang, Y., D. Voskov, M. Khait, and D. Bruhn, 2020, An efficient numerical simulator for geothermal simulation: A benchmark study: Applied Energy, **264**, 114693. (https://doi.org/10.1016/j.apenergy.2020.114693).

Werthmüller, D., W. A. Mulder, and E. C. Slob, 2019, emg3d: A multigrid solver for 3D electromagnetic diffusion: Journal of Open Source Software, **4**, 1463. (https://doi.org/10.21105/joss.01463).

Wu, H., P. Fu, A. J. Hawkins, H. Tang, and J. P. Morris, 2021, Predicting Thermal Performance of an Enhanced Geothermal System From Tracer Tests in a Data Assimilation Framework: Water Resources Research, **57**, e2021WR030987. (https://doi.org/10.1029/2021WR030987).

Zhang, Y., and I. Hoteit, 2021, Feature-Oriented Joint Time-Lapse Seismic and Electromagnetic History Matching Using Ensemble Methods: SPE Journal, **26**, 1341–1365. (https://doi.org/10.2118/203847-PA).

Zhang, Y., F. C. Vossepoel, and I. Hoteit, 2020, Efficient Assimilation of Crosswell Electromagnetic Data Using an Ensemble-Based History-Matching Framework: SPE Journal, **25**, 119–138. (https://doi.org/10.2118/193808-PA).

APPENDIX: ADDITIONAL RESULTS

Introduction

The primary purpose of this appendix is to supplement the limited numerical tests previously reported in the paper. This appendix aims to offer an in-depth exposition of supplementary results, which greatly impacted the selection and execution of the numerical experiments shown in the paper. Unless otherwise stated, the parameters used are the same ones found in the paper.

The main goal of this supplementary analysis is to provide valuable insights for future research work concerning EM monitoring of the DAP well reservoir.

Original source locations

The data assimilation results in the paper were based on five distinct source locations. For brevity, the electric field amplitude ratio plots were omitted. Nevertheless, the inclusion of these fields yields valuable insights, particularly in understanding the utilization of a single receiver in conjunction with multiple sources. For this reason, they are given in this appendix.

The mean electric field amplitude ratio after 25 years are presented in this appendix as Figures A-1a, A-1c, A-1e, A-2a, and A-2c. Correspondingly, Figures A-1b, A-1d, A-1f, A-2b, and A-2d depict the standard deviations of the electric field amplitude ratio.

The first two source locations illustrate the optimal scenario, wherein the proposed receiver location at $x = 1400$ and $y = 1400$ is located in an area with the highest change in electric field amplitude and is also categorized by high standard deviation.

The third source location falls slightly outside the ideal standard deviation range, and the fourth and fifth source location fall outside the ideal mean range and standard deviation range. Despite this, the moments are beyond the range of measurement errors, allowing for these sources to still serve as supplementary constraints on the model's parameters.

By looking at the moments of the electric field amplitude, the source locations can be refined. For instance, increasing the y-coordinate of the third source is likely to increase the standard deviation at the receiver. Furthermore, relocating the fourth and fifth sources to a smaller x-coordinate may potentially yield higher standard deviations at their respective positions.

Emphasizing the highest divergence among ensemble models is crucial, as it gives a greater constraint on models which best best fit the measurement data. This, in turn, enhances the posterior ensemble in representing the subsurface more accurately.

It is also important that the source locations cross the cold plume from different angles, as this allows for stronger constraints within uncertain regions of the cold plume. As is seen in Figures A-2b and A-2d, there is still a high amount of standard deviation at the receiver location, despite the source not being at the direct opposite location of the cold plume. This still allows the EM measurements from these sources to constrain the posterior ensemble.

In the figures it is also seen that the electric field amplitude is slightly different within the -2000 to -2010 m range. This disparity is attributed to a modeling artifact caused by a minor misalignment between the survey domain and the computational domain to which the survey domain is extrapolated.

Source amount

It has been observed that different source locations cause different distributions of the electric field amplitude. Moreover, it has been observed that sources can be placed around the cold plume and still give large differences between ensemble members at a certain receiver well location. These additional measurements can place additional constraints which can assist in reducing the spread of the ensemble members. However, the effect of the source amount on the data assimilation results have not yet been shown properly.

To illustrate the effect of the source amount on the data assimilation results two additional numerical experiments were performed. First, the results on both the temperature at the production well and the temperature field for one single source located at $x = 400$ and $y = 1400$ are given in Figures A-3a and A-3b. Moreover, the results when two more sources are added for a total of three sources are given in Figure A-3c and A-3d. The two additional sources are located at $x = 400$, $y = 1000$ and $x = 400$, $y = 1800$. The results for five sources are given in the paper in Figures 5c and 5d.

As predicted, the inclusion of additional sources improves the temperature forecast of both the production well and the reservoir. In the temperature forecast of the production well it is seen that increasing the amount of sources decreases the spread between ensemble members and also moves the mean of the ensemble closer to the temperature of the reference model. Moreover, the mean temperature field of the ensemble also approaches the reference temperature field, with a decrease in overshoots and undershoots.

One source only provides marginal benefits when compared to the results without EM observations as shown in Figures 5a and 5b. The inclusion of two additional sources already improves the temperature field forecast significantly, using five sources leads to a significant improvement in both the spread and mean of the ensemble of the temperature at the production well forecast and and also further increase the accuracy of the predicted temperature field.

From these observations it can be concluded that using multiple strategically placed source locations is critical to the success of incorporating EM into data assimilation workflow.

Receiver location

It has been established that using multiple strategically placed sources is critical for the success of EM data assimilation. This still leaves the receiver to be decided however. Since the receiver has to be placed in the subsurface, the receiver placement has a far greater cost associated with it due to the requirement of an additional well. This also brings with it the complication that the receiver amount is limited. For this reason two additional experiments are performed using different receiver locations.

The first configuration is one where the receiver is placed at the injection well side at $x = 400$ and $y = 1400$, and the second configuration is one in which the receiver is located below the cold plume spanning between the injection and production well at $x = 1000$ and $y = 1000$. For the first configuration the sources are located at (1400, 1400), (1000, 1000), (1000, 1800), (1400, 1000), and (1400, 1800) with the temperature at the production well and temperature field difference forecast results shown in Figures A-4a and A-4b. The second configuration with the sources located at (500, 2000), (1000, 2000), (1500, 2000), (500, 1400), and (1500, 1400) has the temperature at the production well and temperature field difference results shown in Figures A-4c and A-4d.

Both of these configurations perform slightly worse than the results shown in Figures 5c and 5d. In both cases, the production well forecast, while having a low spread, have a mean which deviates from the actual reference model. The configuration with the receiver placed below the cold plume has a mean which is slightly closer. The temperature difference plots are also slightly worse then the case presented within the paper.

While these results could potentially indicate that the optimal receiver location is at the production well side, there is one significant consideration to be made: the moment analysis of the temperature field was done at 25 years, which was the training period used for the data assimilation. From this the source locations were determined. However, since the sources are located on the surface they are not restricted to stay at the same location for each measurement time during the data assimilation process. For example, for each time step a new set of source locations can be used which are placed to be optimal for the cold plume predicted at that time step. Here the optimal receiver location would be behind the injection well, as this is likely to remain the boundary of the cold plume amongst all time steps as the cold plume moves to the production well.

For this reason, and the observation that different receiver locations are only marginally worse than the setup explored in the paper, the configuration were the receiver is placed behind the injection well is still something which could provide significant value if further explored.

EM observation scaling

The measured electric field amplitude at reservoir depth with a surface source is multiple orders of magnitude smaller than the observations measured at the production well. Without proper scaling, the loss function within ES-MDA will be dominated by the temperature and pressure terms, leading to the EM observations having a reduced impact on the model updates. For this reason the electric field amplitude measurements in the paper were scaled by a factor of 10^{14}, to bring them closer to the production well measurements. However, the effect of using a scaling factor were never shown. To provide more context to this decision two additional experiments were performed using a scaling factor of 10^{12} and 10^{16} on the EM measurements.

To fully understand the effect of the scaling factor on the incorporation of EM measurements an additional metric is used, the scaled EM amplitude observation at the receiver with a source location of $x = 1000$ and $y = 1800$. The reason for using this source location specifically is that the measurements of this source showed the largest change with different scaling factors. Since this measurement has not been shown in the paper, it is hereby given for the scenario presented in Figures 5c and 5d and in Figure A-5.

The temperature at the production well, temperature field difference, and aforementioned scaled EM amplitude observation are shown in Figures A-6a, A-6c, A-6e for a scaling factor of 10^{12}. And in Figures A-6b, A-6d, and A-6f for a scaling factor of 10^{16}.

In all three metrics the scaling factor of 10^{14} performs the best. Moreover, comparing the temperature forecast at the production well between a scaling factor of 10^12 and 10^16 shows that the scaling factor of 10^12 performs better with a lower ensemble spread and better fitting mean. In contrast, the scaling factor of 10^16 has an ensemble with a lesser spread and better fitting mean for the EM measurements. Both scaling factors perform similarly, and slightly worse than the 10^{14} case when the temperature field difference is compared.

As expected, increasing the scaling prioritizes either the production well measurements or EM measurements. However, it is also observed that an optimal scaling factor exists which properly balances the observations to reach a posterior ensemble which performs better in all aspects. For this reason special care should be given to the scaling of the EM measurements, as the difference between the three cases is significant.

An explanation for the relatively similar temperature fields, even when EM measurements are prioritized by a higher scaling, is that the well measurements can still have a significant effect on the loss function. This affects the model updates in the data assimilation to a degree which could negatively affect the final temperature field.

Alpha

ES-MDA is able to achieve multiple data assimilation by using an inflated covariance matrix, where the inflation is controlled by a parameter α_i. This can be seen as replacing one single large correction by multiple smaller corrections.

By decreasing α_i with each assimilation, the covariance matrix becomes increasingly smaller, leading to larger model corrections, and likewise: by increasing α_i with each iteration the covariance matrix becomes increasingly bigger, leading to smaller model corrections.

Two additional numerical experiments are performed to illustrate the effect of this parameter. The results obtained for a decreasing α_i are already shown in Figures 5c and 5d, and in Figure A-5.

The results for a constant α_i, where the values are all 6 are shown in Figures A-7a, A-7c, and A-7e. The results for an increasing α_i, which is the reversed order as seen in the decreasing α_i case, is shown in Figures A-7b, A-7d, and A-7f.

When compared to a constant α_i case, it is observed that decreasing α_i with each iteration gives small but significant improvements to both the temperature prediction of the production well and the field, with no significant improvement seen in the EM observation. Increasing the value of alpha with each iteration decreases the quality of all three metrics significantly compared to the other scenarios.

Training time

An interesting aspect of EM observations seen in Figure A-5 is that even before heat extraction the difference between the ensemble members is significant. This is in contrast to the temperature at the production well measurement, which only shows differences amongst ensemble members after ten years.

The conductivity of the reservoir is heavily influenced by the porosity distribution, and for this reason EM measurements might be able to give improved estimates of the reservoir parameters with a relatively short training time.

It is also important to quantify the usefulness of EM measurements with longer training times, as temperature differences between ensemble members at the production well increase with time, leading to the production well measurements to be able to constrain the model more.

Four additional experiments were performed. Here the data assimilation results only relying on production well measurements and data assimilation results relying on both production well and EM measurements for both 15 and 35 years were simulated. The production well and temperature field difference forecast with 15 years of training time when only production well measurements are used are shown in Figures A-8a and A-8b. Moreover, the results when production well and EM measurements are shown in Figures A-8c and A-8d. Likewise, the results for 35 years are shown in Figures A-8e and A-8f when only production well measurements are relied on, and in Figures A-8g and A-8h when both production well and EM observations are relied on.

It is seen that 15 years only gives a small reduction in the spread of the production well temperature forecast when only well measurements are relied on. In contrast, when EM measurements are also relied on there is a significant improvement in the spread of the ensemble members. Interestingly, the temperature field difference forecast difference when only production well data is relied upon is similar to the case when 25 years are used as seen in Figure 5b, except for the well region showing some improvement. The temperature field difference forecast when EM measurements are incorporated already approaches the results seen with 25 years of training time in Figure 5d.

Comparing the results for 35 years show that EM measurements still improve the forecast at the production well, but only slightly when compared to the case when only well data is relied upon. The temperature field difference forecast using only production well measurements is slightly better than 25 years, but is still worse than the forecast using EM measurements after 15 years. Interestingly, the temperature field difference achieved with EM observations is worse than the one seen at 25 years in Figure 5d. This could be due to a plethora of reason, one of which is that the receiver position was chosen based on the predicted temperature plume at 25 years, or that the scaling of the EM measurements should be changes.

One important consideration is that a simple two- dimensional reservoir model is used which is extrapolated in the third dimension. More realistic scenarios where the overburden also has a complex porosity distribution will affect the ability of EM measurements to predict the reservoir parameter distribution as quickly as seen in these results.

Truncated Gaussian Facies model

The Delft reservoir is fluvial, while the ensemble models used are Gaussian. The reason for using a Gaussian model is that ES-MDA requires is based on the assumption that the models are Gaussian (Emerick and Reynolds, 2013).

A simple method of creating Gaussian models is to adapt the ensemble model generation. Instead of letting the semicovariance use a range a_r which is the same in all directions, the range can instead be defined by the direction. In this case, the y-direction a_r was set to 3000 m, and the x-direction a_r was set to 600 m. This replaces the range a_r with an ellipse which causes structures to be more elongated on the y-axis. Moreover, the Gaussian can be truncated to represent facies. Porosities below 0.15 were set to 0.10, porosities below 0.30 were set to 0.20, and porosities above or equal to 0.30 were set to 0.30. This change from the Gaussian model to a model containing clear facies can be done after the model update from ES-MDA. This maintains Gaussianity while also allowing for more complex models containing facies.

The conductivity for one of these models before and after 25 years of extraction is shown in Figures A-9a and A-9b. Moreover, the resulting conductivity and temperature change are shown in Figures 1c and 1d.

From these figures it is clear that vertical structure are present, which cause the cold plume to travel vertically, rather than mostly horizontally. To show the cold plume path of all ensemble models, the mean and standard deviation of the temperature fields of the entire ensemble after 25 years are given in Figures A-10a and A-10b. Here it is observed that all ensemble models are now more prone to travel vertically, rather than horizontally.

The experiment in the paper is repeated for the ensemble containing facies models. The sources locations were changed to (400, 1400), (400, 1000), (400, 1800), (750, 1500), and (750, 2250). with the receiver well still being located at $x = 1400, y = 1400$. The temperature at the production well temperature and field temperature difference forecast using only production well observations are shown in Figures A-11a and A-11b, production well and EM observations are shown in Figures A-11c and A-11d, and lastly only using EM observations are shown in Figures A-11e and A-11f.

In the 25 year time span, the production well temperature barely changes amongst ensemble members. This causes the results using only EM and production well and EM observation to be similar. EM data is again able to constrain the ensemble members, but this time it becomes less accurate. This is to the mean of the prior ensemble being closer to the reference model temperature forecast. Inspecting the temperature difference forecast plots reveals that utilizing EM data significantly improves the temperature field, despite the temperature field being far more complex. One area is seen where the prediction significantly undershoots the temperature however, which is near the well.

From these figures it is seen that EM observations can resolve even more complex cold plume movements. Moreover, the results are likely to be improved if a better survey design was used. The EM receiver and sources are all located left of the well, causing the well area to not be covered. If the receiver was placed left to the injection closer to the injection well, and the sources were placed on the right at various distances it is possible that even the well area could be accurately resolved.

DISCUSSION AND FUTURE WORK

In this paper it is shown that EM observations are able to greatly improve the data assimilation, causing the model updates to be able to predict the spatial distribution of the cold plume significantly better. Moreover, the combination of production well data and EM data is also able to improve the temperature predictions at the production well.

Nevertheless, this appendix underscores the critical importance of appropriate survey design and meticulous EM observation scaling for the successful integration of EM data. It also highlights several lingering research questions that require further exploration. Substantial additional experimentation is essential to fully quantify the advantages of incorporating EM observations.

One aspect, which has been discussed but not yet experimentally explored, is the use of different sources at different observation time steps. A receiver placed left of the injection well, with the sources moving with the cold front as it expands through time could provide even better data assimilation.

Another noteworthy observation is that the EM measurements between ensemble members is different before extraction. This aspect could also be exploited, and could potentially be leveraged to restrict the prior ensemble before geothermal heat extraction.

Another set of experiments that should be conducted focuses on the influence of observation noise. The low production well observation noise employed in this study may potentially alter some of the outcomes and better underscore the advantages of incorporating EM observations.

Also, the computational intensity of EM simulations necessitated observations only being taken at five-year intervals. However, practical field scenarios allow for both production well and EM observations to be collected monthly or annually. This has the potential to yield even more better outcomes.

It is also important to acknowledge that this paper assumed for there to be no clay in the reservoir. Clay is conductive, and reduces the change in electric resistivity as the temperature decreases. This could reduce the benefit of using EM observations, and should also be quantified.

ES-MDA is inherently limited to Gaussian models, preventing the use of a more realistic fluvial model ensemble that could better depict the Delft reservoir. Techniques do exist for transforming these ensemble models into a Gaussian space. Given the findings in this appendix, which demonstrate the improved forecast performance with more complex reservoir models, it stands to reason that EM observations could similarly enhance predictions when applied to a more representative Delft reservoir model ensemble

Lastly, this paper only showcases two dimensional reservoir models which were extrapolated in the z-axis for the EM forward model. Experiments should also be performed on three-dimensional models, since the effect of vertically changing conductivity is potentially significant.

In conclusion, there is substantial room for methodological refinement, and certain assumptions in this paper may potentially lead to an overestimation of the benefits of EM observations. Nevertheless, the experiments presented in this paper and its appendix underscore the considerable potential of EM observations in subsurface characterization. Their utilization holds significant promise for enhancing decision-making in geothermal planning.

Figures

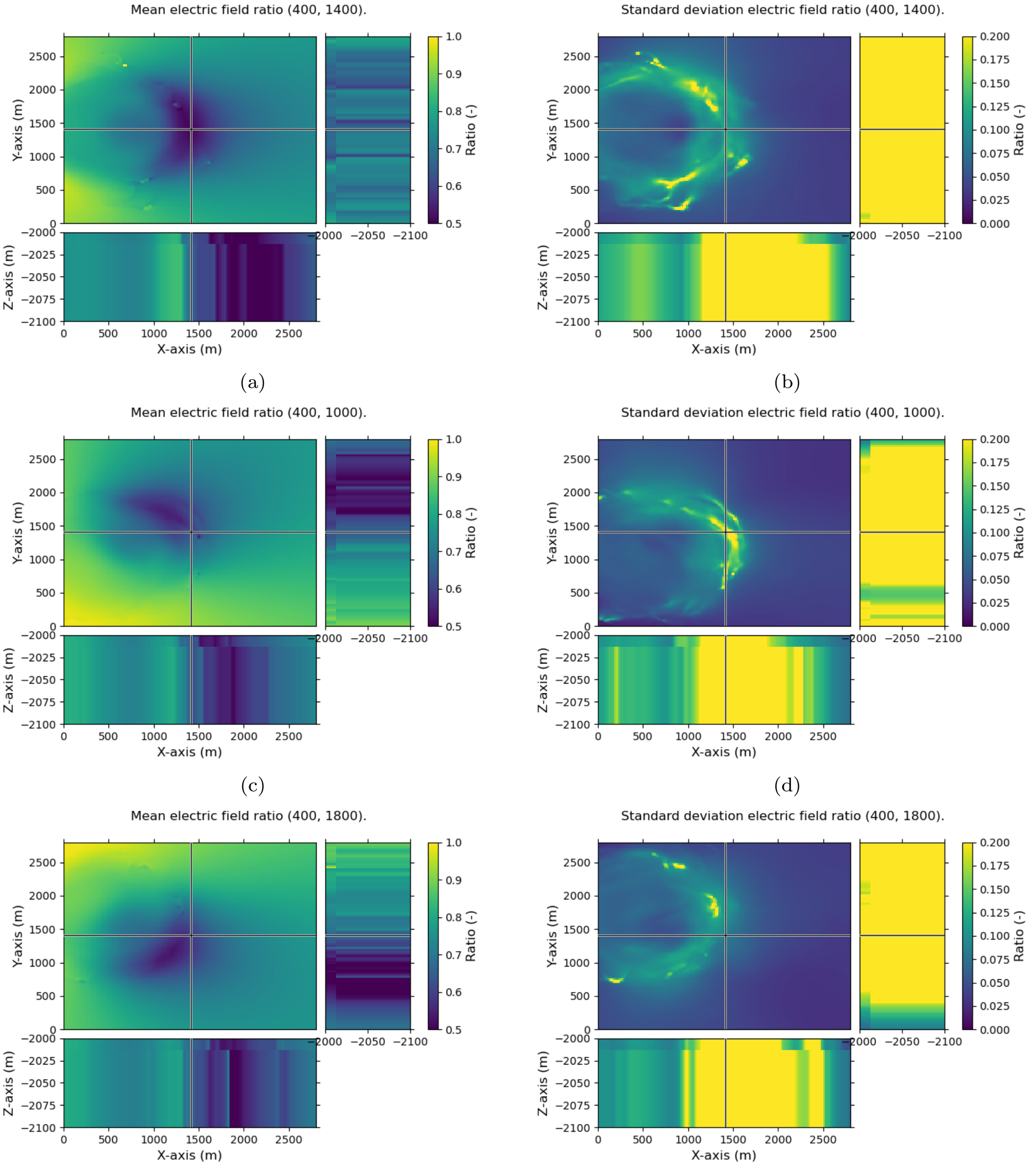
Mean electric field ratio (400, 1400).

Standard deviation electric field ratio (400, 1400).

Mean electric field ratio (400, 1000).

Standard deviation electric field ratio (400, 1000).

Mean electric field ratio (400, 1800).

Standard deviation electric field ratio (400, 1800).

(a) (b)

(c) (d)

(e) (f)

Figure A-1: Mean and standard deviation of the electric field amplitude ratio for the first three source locations. Specifically, with the source location at $x = 400$ and $y = 1400$ (a, b), source location at $x = 400$ and $y = 1000$ (c, d), and source location at $x = 400$ and $y = 1800$ (d, e)

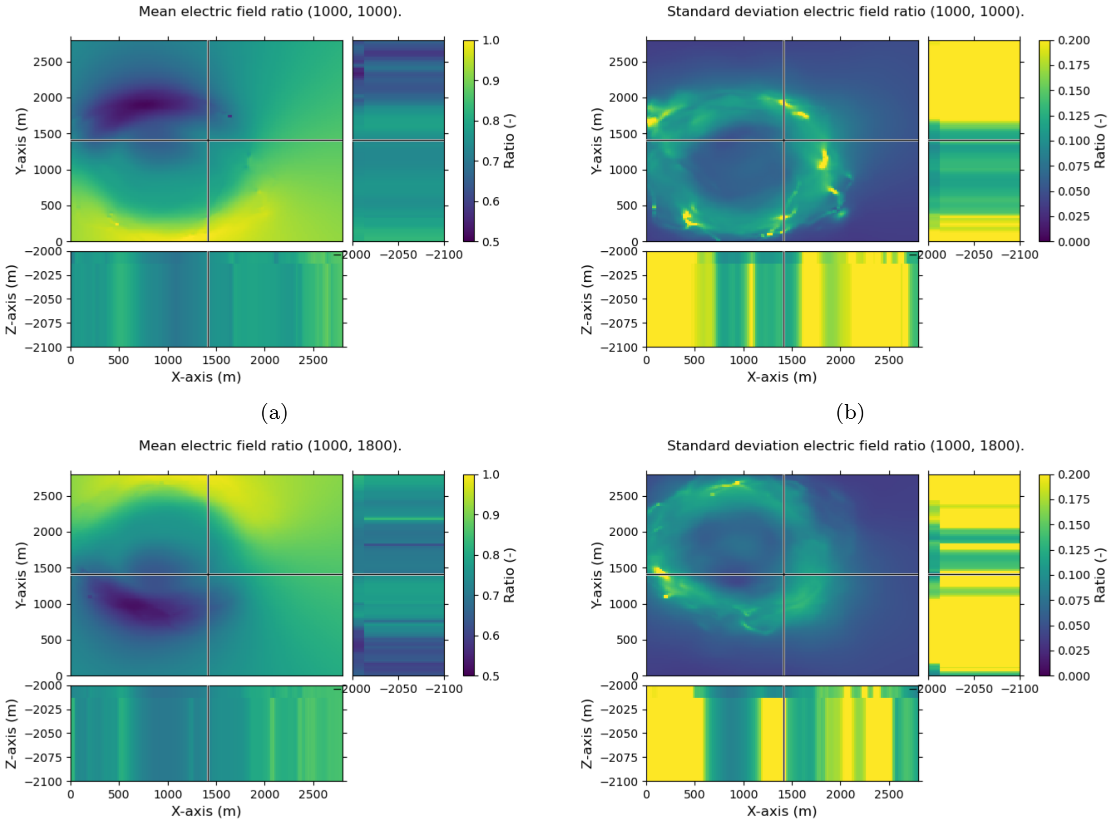

(a) (b)

(c) (d)

Figure A-2: Mean and standard deviation of the electric field amplitude ratio for the last two source locations. Specifically, with the source location at $x = 1000$ and $y = 1000$ (a, b) and source location at $x = 1000$ and $y = 1800$ (c, d).

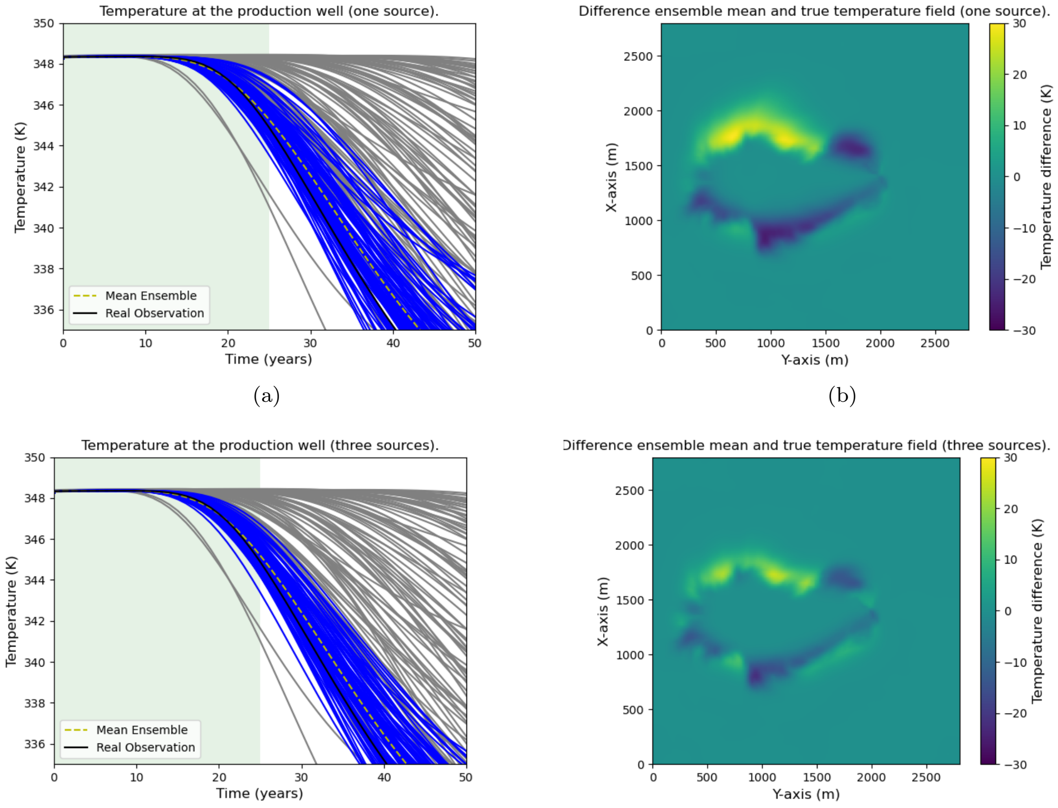

(a) (b)

(c) (d)

Figure A-3: Effect of source amount on the temperature at the production well and temperature field difference forecast. For one source located at $x = 400$ and $y = 400$ (a, b), and for three sources (c, d). In the second case two additional sources were added at $x = 400$ and $y = 1000$, and $x = 400$ and $y = 1800$.

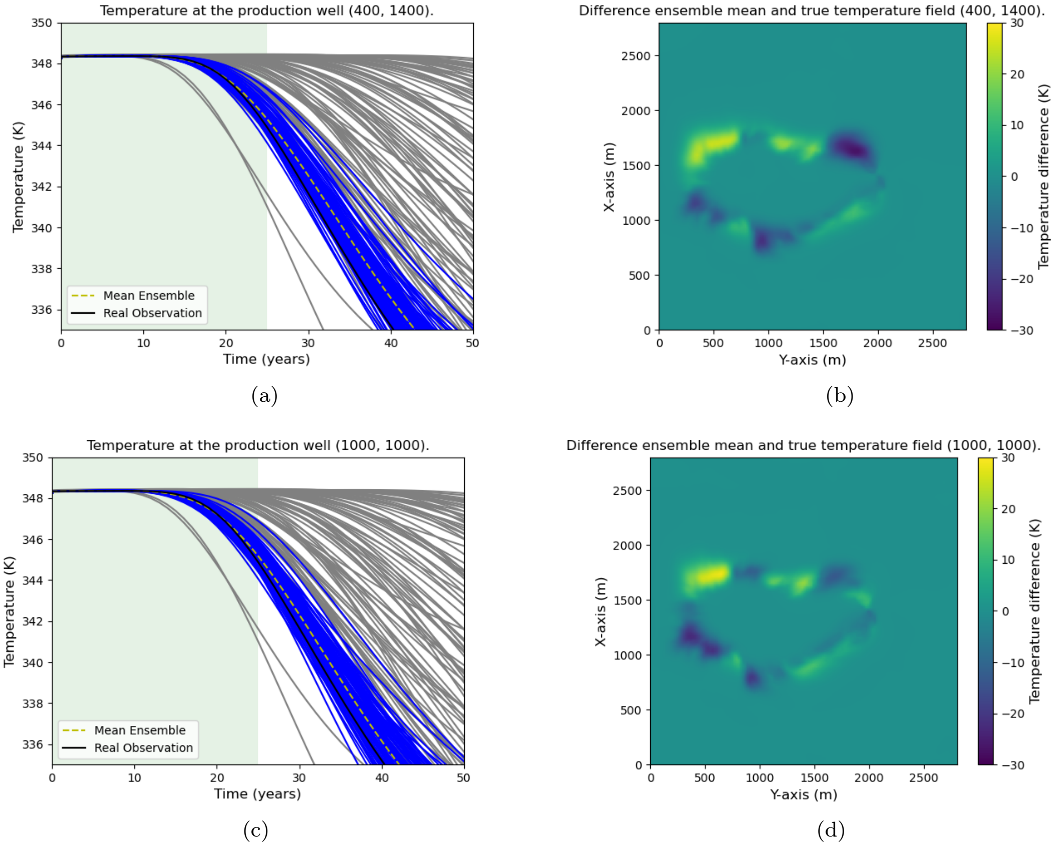
Temperature at the production well (400, 1400).

Difference ensemble mean and true temperature field (400, 1400).

Temperature at the production well (1000, 1000).

Difference ensemble mean and true temperature field (1000, 1000).

(a) (b)

(c) (d)

Figure A-4: Effect of the receiver location on the temperature at the production well and temperature field difference forecast. With the receiver located at $x = 400$ and $y = 1400$, with the sources at (1400, 1400), (1000, 1000), (1000, 1800), (1400, 1000), and (1400, 1800) (a, b). And also with the receiver located at $x = 1000$ and $y = 1000$ and sources at (500, 2000), (1000, 2000), (1500, 2000), (500, 1400), and (1500, 1400) (c, d).

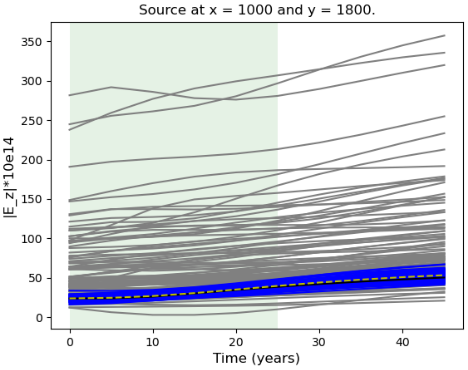

Figure A-5: EM observation with a source at $x = 1000$ and $y = 1800$ and a scaling of EM amplitude by 10^14.

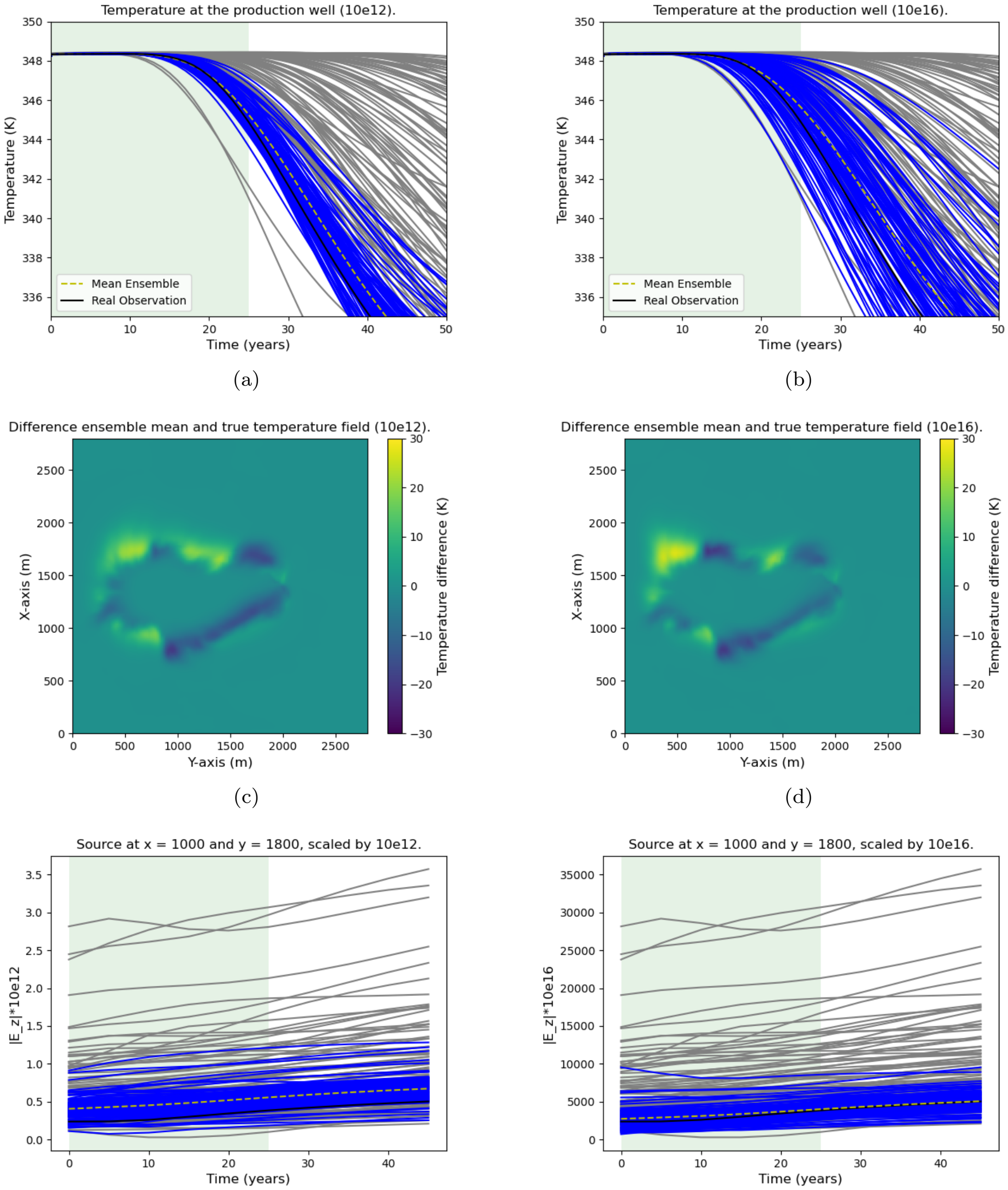

(a) (b)

(c) (d)

(e) (f)

Figure A-6: Effect of the EM amplitude scaling factor on the temperature at the production well, temperature field difference, and EM observation forecast. The EM observation shown is the EM observation when the source is placed at $x = 1000$ and $y = 1800$. The results with a scaling of 10^{12} (a, c, e), and the results with a scaling factor of 10^{16} (b, d, f).

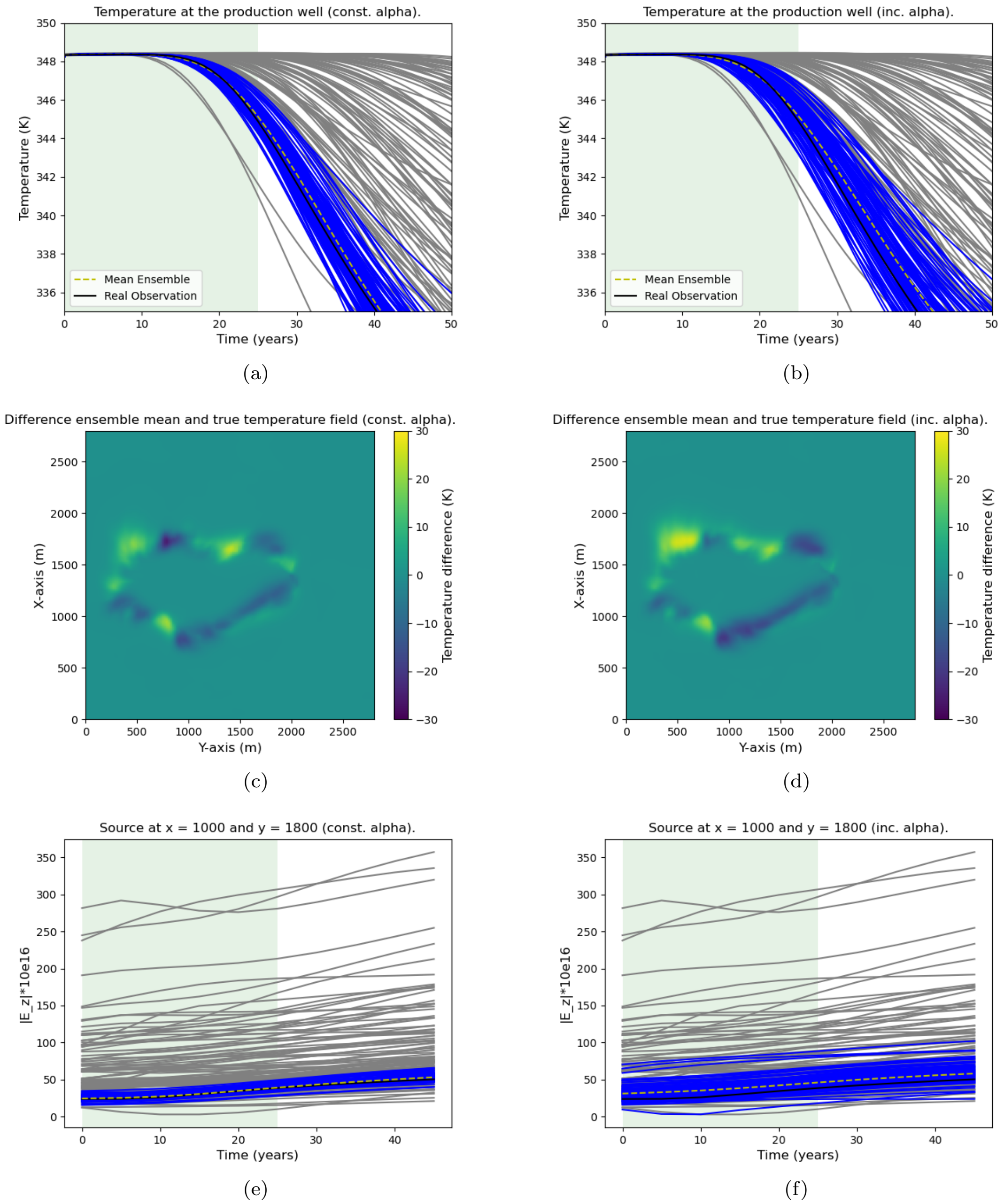

(a) (b)

(c) (d)

(e) (f)

Figure A-7: Effect of the data assimilation parameters α_i on the temperature at the production well, temperature field difference, and EM observation forecast. The results for a constant alpha value (a, b, c) and the results for an increasing alpha (d, e, f) are shown. The results for a decreasing alpha are shown in Figures 5c, 5d, and A-5.

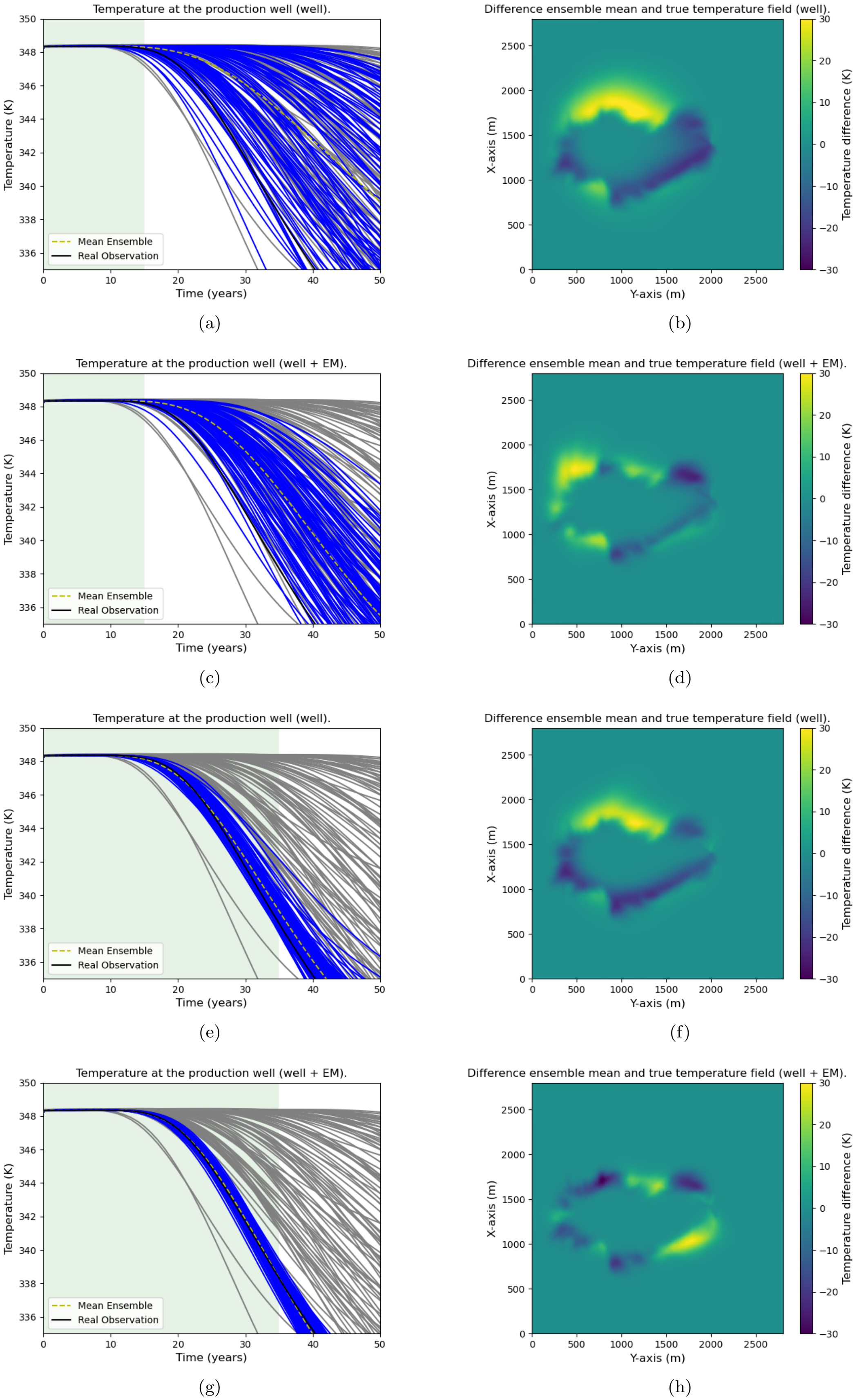

(a) (b)

(c) (d)

(e) (f)

(g) (h)

Figure A-8: Effect of training time on the temperature at the production well temperature and temperature field difference forecast. The results for 15 years of training time with only production well observations (a, b), and with both production well and EM observations (c, d). Likewise, The results for 35 years of training time with only production well observations (e, f) and with both production well and EM observations (g, h).

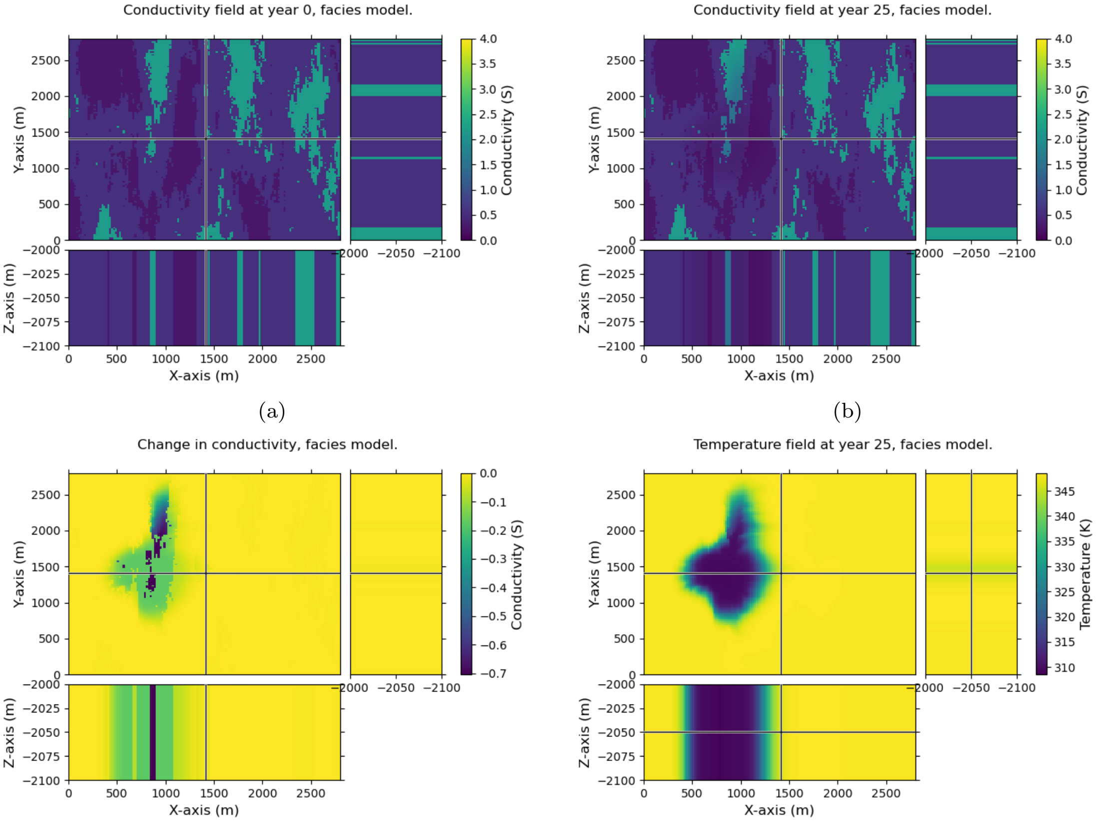

(a) (b)

(c) (d)

Figure A-9: Changes of the conductivity field and temperature field over time for a single facies model. The conductivity field at year 0 in S (a), the conductivity field at year 25 in S (b), the difference between both conductivity fields in S (c), and the temperature field at year 25 in K (d).

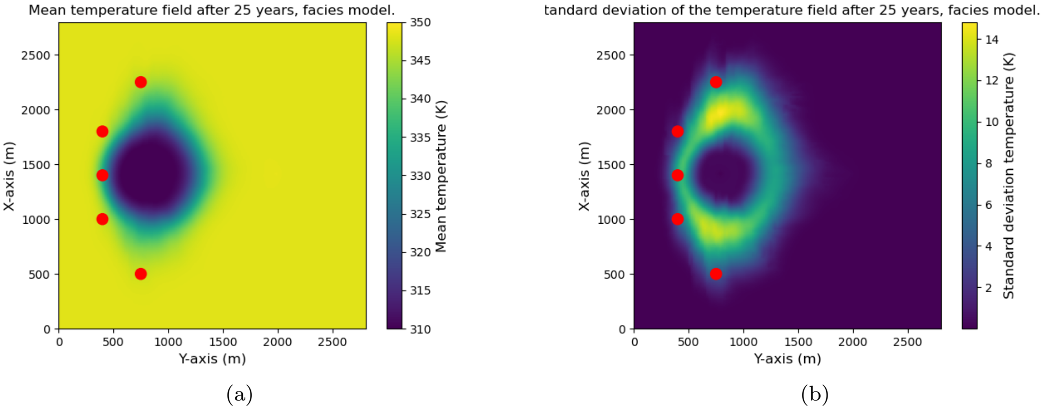

Figure A-10: Mean of the temperature field in K (a) and standard deviation of the temperature field in K (b). The red dots indicate the source positions used.

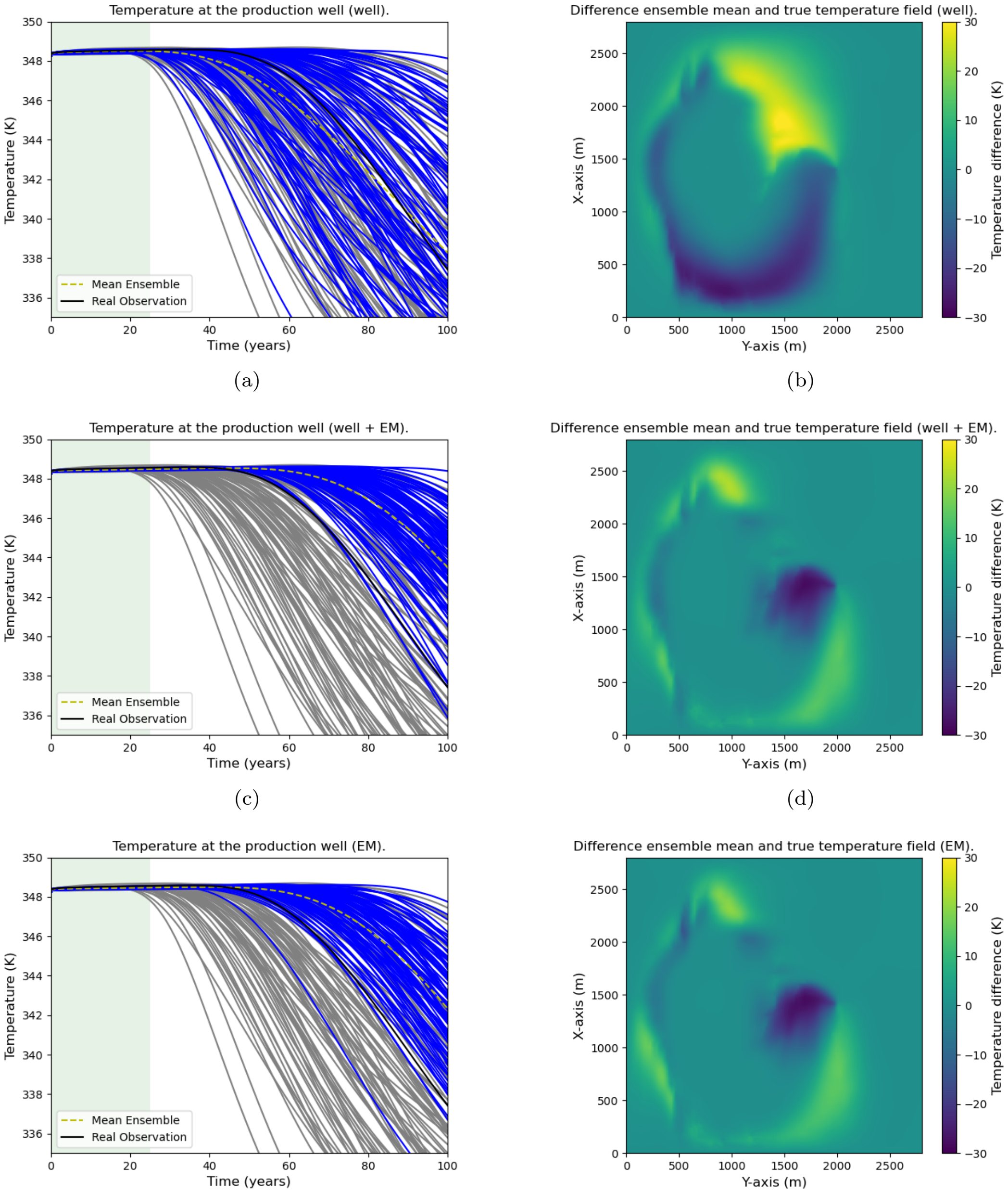

(a) (b)

(c) (d)

(e) (f)

Figure A-11: Data assimilation results for the temperature at the product well and temperature field difference forecast using the ensemble with facies models. The results using only production well observations (a, b), using both production well and EM observations (c, d), and only using EM observations (e, f).